

## Ultrastrong plasmon-phonon coupling in double-layer graphene intercalated with a transition-metal dichalcogenide

Z. H. Tao<sup>1</sup>, E. B. Barros<sup>2</sup>, J. P. da C. Nogueira<sup>2</sup>, F. M. Peeters<sup>1,2</sup>, A. Chaves<sup>2,1</sup>, M. V. Milošević<sup>1,3,\*</sup> and I. R. Lavour<sup>4,1,2,†</sup>

<sup>1</sup>Department of Physics, University of Antwerp, Groenenborgerlaan 171, B-2020 Antwerp, Belgium

<sup>2</sup>Departamento de Física, Universidade Federal do Ceará, Caixa Postal 6030, Campus do Pici, 60455-900 Fortaleza, Ceará, Brazil

<sup>3</sup>Instituto de Física, Universidade Federal de Mato Grosso, 78060-900 Cuiabá, Mato Grosso, Brazil

<sup>4</sup>Instituto Federal de Educação, Ciência e Tecnologia do Maranhão, KM-04 Enseada, 65200-000 Pinheiro, Maranhão, Brazil



(Received 24 April 2023; accepted 14 September 2023; published 28 September 2023; corrected 18 October 2023)

We pursue the premise that plasmon-phonon coupling and hybrid plasmon-phonon modes can be broadly tailored in van der Waals (vdW) heterostructures. While the coupling between optical plasmons in graphene and phonons of substrate materials has already been widely investigated, the coupling of acoustic plasmons to phonons has remained elusive to date. Here we demonstrate that double-layer graphene intercalated with a transition-metal dichalcogenide (TMD) can harbor *acoustic* plasmon-phonon resonances with particularly high coupling strength. Using the quantum-electrostatic heterostructure method, which takes into account the contribution of each vdW monolayer at the *ab initio* level, we present the dependence of the plasmon-phonon coupling strength on the thickness of the TMD, as well as on the graphene doping. Our results reveal optimal and experimentally feasible conditions to achieve ultrastrong plasmon-phonon coupling, and thus enable further advances in nanoscale thermal and optical devices of high sensitivity.

DOI: [10.1103/PhysRevMaterials.7.095201](https://doi.org/10.1103/PhysRevMaterials.7.095201)

### I. INTRODUCTION

The collective excitations of the two-dimensional (2D) electron liquid in graphene, i.e., a 2D honeycomb lattice of carbon atoms [1,2], are known as Dirac plasmons [3]. In the past several years, graphene plasmonics has attracted pertinently increasing research attention, following the discoveries of strong electromagnetic field confinement [3,4], characteristic frequencies tunable by the Fermi energy [5–8], and particularly low losses [9,10]. Relevant to a broad range of optical devices, it was shown that graphene can support plasmons with frequencies from the midinfrared [11–13] to terahertz [7,13–15] range. Furthermore, graphene can be combined with other 2D materials, such as  $MX_2$  transition-metal dichalcogenides (TMDs, e.g.,  $MoS_2$  and  $WS_2$ ), with a metal ( $M$ ) layer between two layers of a chalcogen ( $X$ ) atom, enabling versatile van der Waals heterostructures (vdWhs) [16–18]. It is nowadays possible to precisely control not only constituents, but also their precise stacking in a vdWhs [16,19–24], as well as arrange and adjoin them laterally rather than on top of one another [23–29]. As a result, one may confidently claim the tailored multilayered artificial vdWhs to bolster specific properties and/or desired behavior [18,30]. In that sense, particularly strong advances have been made in optoelectronics [16–19,21,23–31], and graphene plasmonics has emerged as a promising platform for next-generation optoelectronic nanodevices, such as tunable photodetectors [32], mechanical tuning absorbers [33],

optoelectronic switches [34], optical modulators [35,36], and sensors [37,38].

Figures 1(a) and 1(b) illustrate a heterostructure made of  $N$  layers of a TMD material sandwiched inside a double-layer graphene (DLG). When this system is excited by light, a hybrid excitation known as surface plasmon-phonon polariton (SPPP) arises. These quasiparticles emerge when phonons in the TMD are coupled to the electron oscillations in graphene [4]. One of the possibilities to experimentally investigate (excite and measure) the properties of this hybrid excitation is to use scatter-type scanning near-field optical microscopy (s-SNOM) [15,39,40]. This allows one to measure, in the real space, the wavelength of SPPs, with a resolution down to 20 nm [5,6,39–44].

Although TMDs with hexagonal symmetry (2H-TMDs) present four nondegenerate optical phonon modes in the infrared (IR) spectrum at the  $\Gamma$  point, only two of them can couple to Dirac plasmons, via the long-range Fröhlich coupling near the phonon frequencies, namely, the in-plane  $E'$ , which is IR and Raman (R) active, and out-of-plane  $A''_2$  (IR) [19,45–47]. For an even number of stacked TMD layers, the  $E'$  and  $A''_2$  modes of 1L- $MX_2$  split into  $E_u$  (IR) and  $E_g^1$  (R), and  $A_{2u}$  (IR) and  $A_{1g}^1$  (R) modes, respectively [45]. For bulk  $MX_2$  on the other hand,  $A''_2$  splits into  $A_{2u}$  (IR) and  $B_{2g}^1$  modes, where the latter is optically inactive (silent). Figure 1(c) illustrates the described evolution of the  $A''_2$  mode from a single layer to the  $MX_2$  bulk case. For more details and a complete description of  $N$ -layer 2H-TMD phonon modes at the  $\Gamma$  point, we refer the reader to Refs. [21,47].

Recently, graphene-based systems with coupled plasmon-phonon polaritons have been proven useful for near-field

\*milorad.milosevic@uantwerpen.be

†icar@fisica.ufc.br

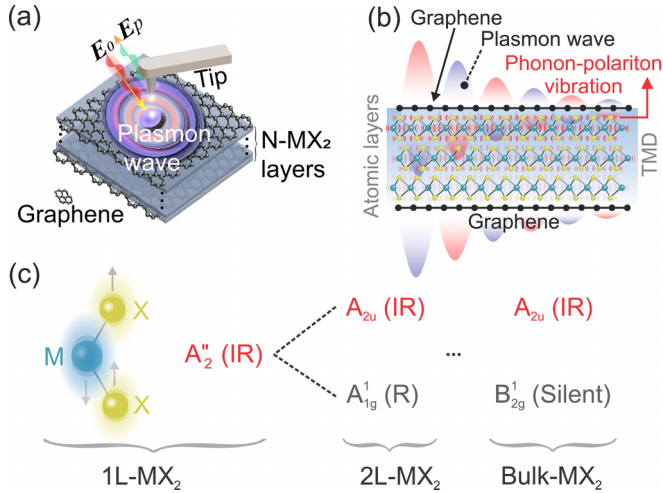


FIG. 1. (a) Schematic illustration of the scatter-type scanning near-field optical microscopy setup and a Dirac plasmon wave in a van der Waals heterostructure (vdWhs) composed of  $N$ - $MX_2$  ( $M = \text{Mo}, \text{W}; X = \text{S}, \text{Se}$ ) layers encapsulated by two graphene (G) monolayers. (b) Lateral view of the  $G/3$ - $MX_2/G$  vdWhs, illustrating the hybridization of the TMD phonon vibration with Dirac plasmon in graphene, giving rise to surface plasmon-phonon polaritons (SPPPs). (c) Schematic representation of the out-of-plane  $A_2''$  phonon mode in a  $MX_2$  monolayer. For an even number of TMD layers, the  $A_2''$  mode splits into  $A_{2u}$  (IR) and  $A_{1g}^1$  (R). For the bulk  $MX_2$ ,  $A_2''$  splits into  $A_{2u}$  (IR) and  $B_{2g}^1$ , where the latter is silent for excitations. Here, IR and R stand for infrared and Raman, respectively.

radiative heat transfer, which may improve the heat dissipation capacity of nanodevices [48–50]. Furthermore, previous works on double layers have shown that electric fields of the plasmons of the two plasmonic interfaces will couple and split plasmon modes into two, namely, the optical and the acoustic modes [51–55]. One of the advantages of using DLG-based vdWhs is that one can have a dual-gate control of the carrier density individually in either graphene layer, and the possibility to control interlayer interactions by introducing another 2D material between the graphene monolayers, yielding novel electronic and optical properties. More recently, acoustic plasmons were visualized in real space in large-area graphene, truly opening technological possibilities to use acoustic plasmons in graphene-based optoelectronics and sensing applications [56].

Motivated by the above facts, in this paper we have designed a double-layer graphene-based vdWhs, illustrated in Figs. 1(a) and 1(b), aimed at enhancing and tuning the coupling of *acoustic* Dirac plasmons of graphene to the out-of-plane IR-active  $A_2''$  phonon mode of the TMD inside the DLG. To characterize the desired coupling and the resultant properties, we used realistic simulations at the level of density function theory (DFT) and many-body perturbations, combined with the quantum electrostatic heterostructure (QEH) model. We thereby identify the way in which the coupling between acoustic Dirac plasmons and out-of-plane IR-active  $A_2''$  phonon modes of  $\text{MoS}_2$  and  $\text{WS}_2$  takes place, and how it depends on the number of TMD layers put between the graphene ones. We further reveal that doping of graphene layers can be used to broadly tune the coupling strength,

enabling the versatile design of optoelectronic and thermal nanodevices.

As shown in Ref. [57], the acoustic Dirac plasmon in graphene couples mostly to the out-of-plane IR-active  $A_2''$  TMD phonon; hence, in this work, we maintain the focus on the coupling to that particular mode. We, however, consider double-layer graphene in order to generate an interlayer plasmon-plasmon interaction, thereby increasing the magnitude of the confined perpendicular electric field mode [58–60], and, consequently, further enhancing the acoustic Dirac plasmon coupling to the out-of-plane IR-active  $A_2''$  TMD phonon mode.

The paper is organized as follows. In Sec. II, we introduce the random phase approximation (RPA) theory of plasmons in spatially separated double-layer graphene and of hybrid plasmon-phonon polaritons modes. In Sec. III, we present the results of the plasmon-phonon dispersion in the  $(q, \omega)$  plane obtained from the QEH model, emphasizing the way we calculate the plasmon-phonon coupling strength ( $\Omega$ ) at the minimum energy splitting (MES). Then, we show the dependence of the SPPP's coupling strength on the number of TMD layers, for the acoustic plasmons and IR-active out-of-plane  $A_2''$  phonon mode, and identify weak-coupling (WC), strong-coupling (SC), and ultrastrong-coupling (USC) regimes, via the normalized coupling parameter  $\eta$ . Finally, we discuss how the doping of graphene and the consequently varied Fermi energy affect the coupling strength. The summary of our findings and conclusions is provided in Sec. IV.

## II. THEORY OF PLASMONS IN DOUBLE-LAYER GRAPHENE AND HYBRID PLASMON-PHONON POLARITONS MODES

Dirac plasmons, defined as density oscillations of Dirac-like low-energy electrons in graphene, can be obtained from the total dielectric function of the system within the random phase approximation (RPA) [60–62]. For a double-layer graphene system, the collective plasmon modes are obtained by solving the plasmon equation, which corresponds to the zeros of the generalized dielectric tensor  $\epsilon_{ij}(q, \omega)$  [51,63],

$$\epsilon_{ij}(q, \omega) = \delta_{ij} - v_{ij}(q)\chi_j(q, \omega) = 0, \quad (1)$$

where  $i, j = 1$  or  $2$  denote the two graphene layers. From Eq. (1), the two-component determinant equation becomes

$$\epsilon(q, \omega) = [1 - v_{11}(q)\chi_1(q, \omega)][1 - v_{22}(q)\chi_2(q, \omega)] - v_{12}(q)v_{21}(q)\chi_1(q, \omega)\chi_2(q, \omega), \quad (2)$$

where  $\chi_1$  ( $\chi_2$ ) is the noninteracting density-density response function of the top (bottom) graphene layer. Since the dielectric environment consists of three contacting media with different dielectric constants  $\epsilon_1$  ( $z < 0$ ),  $\epsilon_2$  ( $0 < z < d$ ), and  $\epsilon_3$  ( $z > d$ ), the Coulomb 2D Fourier transform of the electron-electron interaction can be defined as [63]

$$v_{ij}(q, d) = \frac{2\pi e^2}{q\epsilon_{ij}(qd)}. \quad (3)$$

Here,  $\epsilon_{ij}$  accounts for the three effective dielectric functions defined as

$$\frac{1}{\epsilon_{11}(q)} = \frac{2(\epsilon_2 \cosh qd + \epsilon_3 \sinh qd)}{\epsilon_2(\epsilon_1 + \epsilon_3) \cosh dq + (\epsilon_1 \epsilon_3 + \epsilon_2^2) \sinh qd}, \quad (4a)$$

$$\frac{1}{\epsilon_{22}(q)} = \frac{2(\epsilon_2 \cosh qd + \epsilon_1 \sinh qd)}{\epsilon_2(\epsilon_1 + \epsilon_3) \cosh dq + (\epsilon_1 \epsilon_3 + \epsilon_2^2) \sinh qd}, \quad (4b)$$

$$\frac{1}{\epsilon_{12}(q)} = \frac{2\epsilon_2}{\epsilon_2(\epsilon_1 + \epsilon_3) \cosh dq + (\epsilon_1 \epsilon_3 + \epsilon_2^2) \sinh qd}. \quad (4c)$$

From Eq. (3), the intra- and interlayer Coulomb interaction matrix elements are given by  $v_{ii}$  and  $v_{ij}$ , respectively, where  $i, j = 1, 2$  are again the graphene monolayer indices. In order to facilitate the understanding of the plasmonic dispersion in the DLG system, we assume that the optical and acoustic plasmon dispersion attain, respectively, their long-wavelength forms, defined as [63]

$$\omega_{OM}(q) = \sqrt{\frac{ge^2 v_F k_F}{\epsilon_{13}}} q \quad (5a)$$

and

$$\omega_{AM}(q) = \frac{1 + q_{TF} d}{\sqrt{1 + 2q_{TF} d}} v_F q, \quad (5b)$$

where  $\epsilon_{13} = (\epsilon_1 + \epsilon_3)/2$ ,  $g = 4$  represents the spin and valley degeneracy in graphene,  $q_{TF} = ge^2 k_F^2 / (\epsilon_2 E_F)$  is the Thomas-Fermi screening wave vector in graphene, and  $k_F$  ( $E_F = v_F k_F$ ) is the Fermi wave vector (Fermi energy). Thus, from Eqs. (5a) and (5b), the well-known characteristic square-root dispersion [ $\omega_{OM}(q) \propto \sqrt{q}$ ] of the optical plasmon mode and the linear dependence [ $\omega_{AM}(q) \propto q$ ] of the acoustic plasmon mode can be observed. As discussed in Ref. [57], the concept of plasmon-phonon coupling can be understood from the basis of two simple coupled classical harmonic oscillators, where the hybrid plasmon-phonon modes are given by

$$\omega_{\pm}^2 = \frac{1}{2} [\omega_{ph}^2 + \omega_{pl}^2 \pm \sqrt{(\omega_{ph}^2 - \omega_{pl}^2)^2 + 4\Omega^2 \omega_{ph} \omega_{pl}}]. \quad (6)$$

In Eq. (6),  $\omega_{ph}$  is the TMD phonon frequency, while  $\omega_{pl}$  is the plasmon dispersion which can be replaced by Eq. (5a) or Eq. (5b).  $\Omega$  plays the role of the coupling energy associated with the interaction between the TMD phonons and the optical or acoustic Dirac plasmons.

### A. Computational method

The quantum-electrostatic heterostructure (QEH) model [64] is employed to calculate the plasmonic properties of the vdWhs represented in Figs. 1(a) and 1(b). This accurate computational method is a DFT-based technique that takes into account the screening from electronic transitions at the level of the random phase approximation (RPA), where the active TMD phonon contribution of the 2D layers, screening from homogeneous bulk substrates, and the graphene doping contributions are treated with *ab initio* precision [64–66].

One of the major advantages of this method is that QEH calculates the total dielectric properties of the vdWhs with layer-by-layer precision since the contribution of each layer is considered separately. Over the last few years, QEH has

been demonstrated as a very useful tool for theoretical plasmonic investigations, in various heterostructures [65–69], mostly yielding experimentally realistic results. For example, Ref. [67] presented an excellent agreement between the QEH and experimental results on heterostructures composed of graphene and hexagonal boron nitride (hBN). The authors employed the QEH method to demonstrate the possibility to probe the structure and composition of different vdWhs using graphene on top of different TMDs through the sensitivity of the graphene plasmons to the dielectric environment (changing, consequently, the plasmon wavelength).

Another important advantage of the QEH model is its integration with the Computational 2D Materials Database (C2DB) [70,71], a vast database containing the dielectric building blocks (DBBs) of 2D materials [72]. Therefore, using the C2DB results, which were previously obtained with thorough *ab initio* calculations, allows us to detail the effects of the coupling of acoustic plasmons that arise in a double-layer graphene system [60], to active TMD phonon modes in a vdWhs, without the need to treat the dielectric environment as slabs of bulk material. The fundamental assumption behind the QEH model is the additivity of independent polarizabilities of individual layers. Therefore, in plasmon-phonon coupling, the QEH model does not encompass the effects of phonon renormalization and shift. However, this approximation, remarkably accurate when there is no hybridization between neighboring layers' wave functions, remains valid even in the presence of interlayer hybridization [65]. Furthermore, the QEH model is in excellent agreement with s-SNOM experimental results [67].

Finally, to identify the acoustic plasmon-phonon coupling strength  $\Omega$ , we analyze the loss function, defined as  $L = -\text{Im}1/\epsilon(q, \omega)$ , obtained from realistic calculations using the QEH model. In this case, due to the hybridization between the acoustic plasmon and the TMD phonon, an anticrossing between the top [ $\omega_+(q)$ ] and bottom [ $\omega_-(q)$ ] hybrid modes emerges, close to the phonon frequency. Therefore, the coupling strength can be calculated from the minimum energy splitting as [57]

$$\Omega = \frac{1}{2} [\omega_+(q) - \omega_-(q)]_{\min}, \quad (7)$$

where  $\omega_+(q)$  and  $\omega_-(q)$  are the frequencies of the top and bottom hybrid plasmon-phonon modes. For the sake of completeness, here we summarize the main aspects behind the QEH calculations based on Refs. [64] and [65]. For more details and a complete description, please see the respective references and their supplemental materials.

To calculate the loss function and plasmon dispersion of the vdWhs, the QEH numerically couples the density-density response function of each the  $i$ th layer  $\chi_i(z, z', \mathbf{q}_{\parallel}, \omega)$ , present in the DBBs of the C2DB. To obtain the total function of the entire heterostructure, the QEH method couples each single layer together, i.e., the DBBs, through the long-range Coulomb interaction by solving a Dyson-like equation. Therefore, the Dyson equation of the total density-density response function of the complete vdWh is given by [64]  $\chi_{i\alpha, j\beta} = \chi_{i\alpha} \delta_{i\alpha, j\beta} + \chi_{i\alpha} \sum_{k \neq i, \gamma} V_{i\alpha, k\gamma} \chi_{k\gamma, j\beta}$ , where, for simplicity, the  $\mathbf{q}_{\parallel}$  and  $\omega$  variables were omitted.  $\alpha = 0, 1$  represents the monopole and dipole components, respectively, and the Coulomb matrices are defined as  $V_{i\alpha, k\gamma}(\mathbf{q}_{\parallel}) =$

TABLE I. Optical phonon frequencies for the freestanding monolayer of MoS<sub>2</sub> and WS<sub>2</sub> considered in the QEH calculations. The vibrational optical phonon modes of their monolayers are represented by  $E''$  (R),  $E'$  (IR and R),  $A'_1$  (R) and  $A'_2$  (IR), where IR (R) means that the mode is active for infrared (Raman) excitations [45,84–86,93,94].

	Phonon frequencies (meV)			
	1 ( $E''$ )	2 ( $E'$ )	3 ( $A'_1$ )	4 ( $A'_2$ )
MoS <sub>2</sub>	34.19	46.35	47.59	56.16
WS <sub>2</sub>	35.56	42.85	50.12	51.00

$\int \rho_{i\alpha}(z, \mathbf{q}_{\parallel}) \Phi_{k\gamma}(z, \mathbf{q}_{\parallel}) dz$ , where  $\Phi_{k\gamma}(z, \mathbf{q}_{\parallel})$  is the potential created by the density profile,  $\rho_{k\gamma}(z, \mathbf{q}_{\parallel})$ . Using this formalism, the inverse tensorial dielectric function of the vdWh reads

$$\epsilon_{i\alpha, j\beta}^{-1}(\mathbf{q}_{\parallel}, \omega) = \delta_{i\alpha, j\beta} + \sum_{k\gamma} V_{i\alpha, j\beta}(\mathbf{q}_{\parallel}) \chi_{k\gamma, j\beta}(\mathbf{q}_{\parallel}, \omega). \quad (8)$$

Consequently, the loss function can be found through

$$L(\mathbf{q}_{\parallel}, \omega) = -\text{Im}\{\text{Tr}[\epsilon^{-1}(\mathbf{q}_{\parallel}, \omega)]\}. \quad (9)$$

Finally, from Eq. (9), collective modes, such as the plasmon dispersion, are obtained as the maxima of the loss function.

One important effect in vdWhs occurs when TMD phonons couple to surface plasmon-polaritons (SPPs). In this case, nontrivial effects in the  $(q, \omega)$  dispersion are originated, giving rise to one or more hybrid regions, i.e., mixed region(s) with plasmon and phonon dispersion mixed, resulting in a surface plasmon-phonon-polaritons (SPPPs). To compute this important phenomenon, i.e., the phonon contribution of each 2D material, it is necessary to include in the computational model [65] the  $\Gamma$ -point phonon modes of the individual layers and the Born effective charges. The first contribution is presented in Table I, while the Born effective charges are defined as tensors that give the proportionality between the variation of the 2D polarization density  $P_i$ , due to an atomic displacement, defined as  $Z_{i,aj} = \frac{A_{\text{cell}}}{e} \frac{\partial P_i}{\partial u_{aj}}|_{E=0}$ . Here, the  $A_{\text{cell}}$  is the in-plane area of the 2D layer,  $a$  denotes an atom, and  $i$ - $j$  are Cartesian coordinates [65]. Subsequently, the lattice polarizability of a 2D material in the optical limit ( $\mathbf{q} = 0$ ) can be obtained through [65]

$$\alpha_{ij}^{\text{lat}}(\omega) = \frac{e^2}{A_{\text{cell}}} \sum_{ak, bl} Z_{i,ak} \{[\mathbf{C} - \mathbf{M}(\omega^2 - i\gamma\omega)]^{-1}\}_{ak, bl} Z_{j,bl}, \quad (10)$$

where  $\mathbf{C}$  is the force constant matrix in the optical limit,  $\mathbf{M}$  is a diagonal matrix containing the atomic masses, and the broadening parameter  $\gamma$  is set to 10 meV [71], representing the phonon lifetime [see the supporting information of Ref. [65] for a derivation of Eq. (10)].

Thus, considering the contributions of electrons and phonons, the total monopole and dipole components of the DBB of layer  $i$  are defined as [65]

$$\chi_{i0}^{\text{total}}(\mathbf{q}_{\parallel}, \omega) = \chi_{i0}^{\text{el}}(\mathbf{q}_{\parallel}, \omega) - \mathbf{q}_{\parallel}^2 \alpha_{\parallel}^{\text{lat}}(\omega), \quad (11a)$$

$$\chi_{i1}^{\text{total}}(\mathbf{q}_{\parallel}, \omega) = \chi_{i1}^{\text{el}}(\mathbf{q}_{\parallel}, \omega) - \alpha_{zz}^{\text{lat}}(\omega), \quad (11b)$$

where  $\alpha_{\parallel}^{\text{lat}}$  denotes the  $2 \times 2$  in-plane submatrix of  $\alpha^{\text{lat}}$ . All DBBs in this work are from the C2DB project. The electronic polarizability  $\chi_{i0}^{\text{el}}$  calculation is based on the random phase approximation (RPA) [70], while lattice polarizability  $\alpha_{ij}^{\text{lat}}$  is calculated in the recent progress of the C2DB [71] and Ref. [65].

## B. The coupling strength regime

In order to investigate how significant the plasmon-phonon hybridization is, it is necessary to compare the plasmon-phonon coupling strength ( $\Omega$ ) to other relevant energy scales, for example, the phonon energy ( $\hbar\omega_{ph}$ ) and the linewidth of the coupled system [73]. In this situation, the splitting becomes significant only when the coupling  $\Omega$  exceeds the linewidths of the coupled systems, which also enables the experimental observation of these two modes. Thus, if  $\Omega$  is very small compared to other important energy scales, for example, the phonon energy, the coupling is negligible and is not strong enough to change the original (uncoupled) frequencies. This defines different coupling regimes. The first one, where  $\Omega$  can effectively be neglected, is classified as weak coupling (WC) [73,74]. On the other hand, if the strength of the plasmon-phonon coupling is large enough to modify the uncoupled energy dispersion, thus creating hybrid plasmon-phonon modes, the coupling regime can be classified as strong (SC) [73,74]. The stronger coupling reflects more efficient plasmon-phonon interactions, which is crucial for many applications based on, or mediated by, hybrid states [75–77]. In this article, we define the coupling regimes in a pragmatic way, after normalizing the coupling strength to the phonon frequency at the source of hybridization, as  $\eta = \Omega/\hbar\omega_{ph}$ . Then, the WC regime corresponds to  $\eta < 0.01$ , and the SC regime to  $\eta \geq 0.01$ . In addition, and as discussed in Ref. [75], we define the ultrastrong coupling (USC) regime for  $\eta \geq 0.1$ , where plasmon-phonon coupling not only alters the characteristic energy dispersion, but may radically change the observable properties of the system [78].

## C. Electric field profile in double-layer graphene intercalated with a TMD

Interaction between confined modes localized at each of the two interfaces in the DLG system forms coupled modes. To show the electric field profile of such coupled modes in TMD-intercalated double-layer graphene, the finite-element method (FEM) is used to perform full-wave simulations. In these simulations, the TMD-intercalated double-layer graphene is placed in the center of the computational domain, surrounded by a perfectly matched layer. Graphene can be considered as a conducting interface [79], or a boundary condition that sustains the confined electronic-magnetic field mode, with a simple Drude surface conductivity, as [80]

$$\sigma(\omega) = \frac{e^2 E_F}{\pi \hbar^2} \frac{i}{\omega + i\tau^{-1}}. \quad (12)$$

In Eq. (12), we consider  $E_F = 100$  meV as the Fermi level of the graphene and  $\tau \sim 10^{-13}$  s as the relaxation time for electrons. Under a normal-incidence plane-wave  $\mathbf{E} = E_0 e^{i(k_0 z - \omega t)} \hat{x}$ , the  $x$  and  $z$  components of the electric fields are

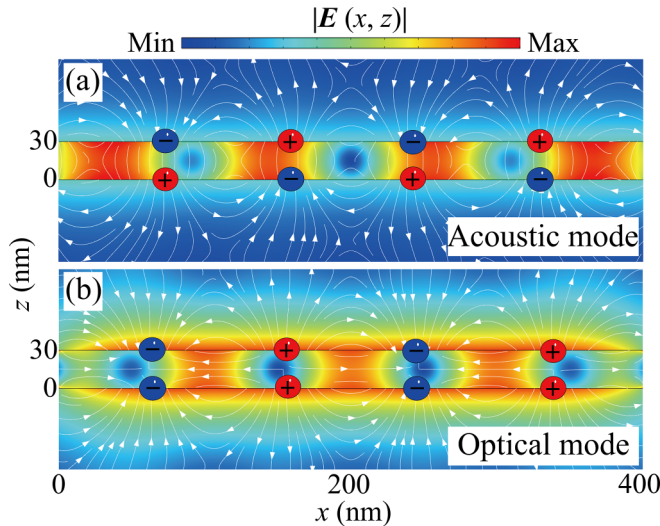


FIG. 2. Schematic illustration of the electric field lines  $\mathbf{E}(x, z)$  in a double-layer graphene system, with the color map showing the normalized magnitude of the field  $[|\mathbf{E}(x, z)|]$ . The top and bottom layers are separated by  $d = 30$  nm. For simplicity, the dielectric constant of the top and bottom layers is  $\epsilon_1 = \epsilon_2 = 1$ , and in between, it is  $\epsilon_3 = 4$ . (a) The acoustic mode (AM) and (b) the optical mode (OM). The positive (red circles) and negative (blue circles) charges represent, qualitatively, the formation of dipolelike charges. For the AM, the electric fields in between the layers (red regions) increase the coupling of the plasmons to the out-of-plane optical phonon modes.

plotted in Fig. 2, considering a TMD thickness  $d = 30$  nm, representing the distance between two graphene layers.

### III. RESULTS AND DISCUSSION

#### A. Overview of plasmon-phonon dispersion in double-layer graphene-based vdWhs

Figure 3(a) shows the loss function obtained from the QEH for a G/10-MoS<sub>2</sub>/G heterostructure. In this figure, one observes that the plasmon dispersion presents both optical ( $\hbar\omega_{OM} \propto \sqrt{q}$ ) and acoustic ( $\hbar\omega_{AM} \propto q$ ) surface plasmon-phonon polaritons (SPPPs), and four MoS<sub>2</sub> phonon modes [the last mode is magnified in the inset of Fig. 3(b)]. It is also possible to observe, from the loss function, a well-defined split mode (anticrossing) for the coupling between the acoustic plasmon mode (AM) and  $A_2''$  phonon mode, in contrast to the optical mode (OM). This means that the coupling is much stronger for the acoustic than for the optical case. Since our interest is in the acoustic plasmon-phonon coupling, Fig. 3(b) emphasizes the plasmon dispersion close to the hybridization region. Figure 3(c) shows a magnification of the square box marked in Fig. 3(b). From this panel, two clearly split hybrid modes are seen, labeled as  $\omega_+$  and  $\omega_-$ , where the point of minimum energy difference between them gives us the coupling strength  $\Omega$ , as presented in Fig. 3(d). The dashed white line in Figs. 3(b) and 3(c), used for reference, represents the surface plasmon polariton (SP<sup>2</sup>) dispersion without considering the phonon contribution, i.e., taking into account only the dielectric contributions of the TMD.

Under the same excitation momentum, the frequency of the acoustic mode is lower, that is, closer to the phonon

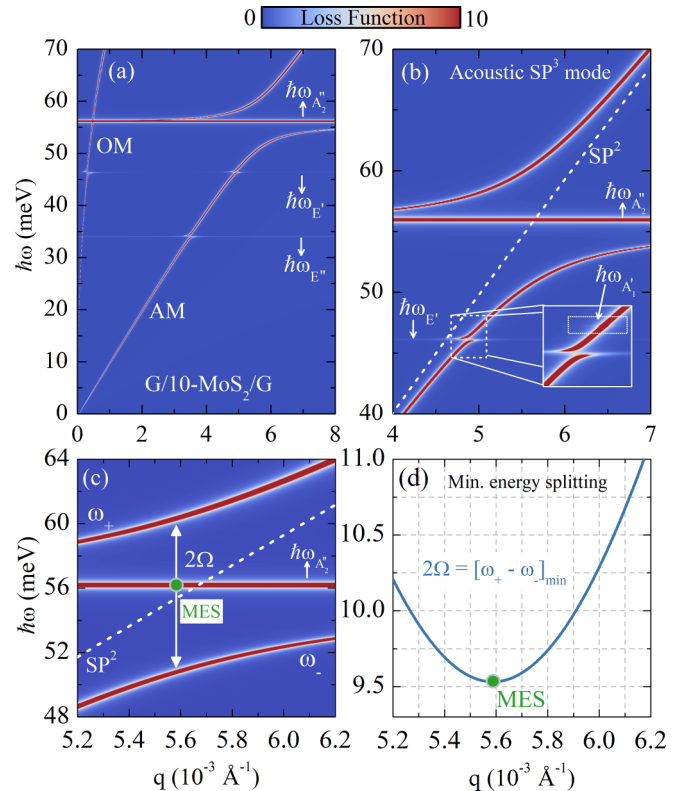


FIG. 3. (a) Loss function of the surface plasmon-phonon polariton dispersion for a G/10-MoS<sub>2</sub>/G vdWhs with  $E_F = 150$  meV. OM and AM indicate the optical and acoustic Dirac plasmon modes, respectively. Horizontal branches in the loss function are signatures of the four MoS<sub>2</sub> phonon modes, labeled  $E''$  (R),  $E'$  (IR and R),  $A_1'$  (R) [see magnification in (b)] and  $A_2''$  (IR). IR (R) means that the mode is active for infrared (Raman) excitations. (b) The same as in (a), but now emphasizing the coupling between the acoustic Dirac plasmons mode (AM) and the MoS<sub>2</sub> phonon modes. (c) Magnification close to the IR-active  $A_2''$  phonon mode, where two well-defined hybrid modes  $\omega_+$  and  $\omega_-$  arise due to the plasmon-phonon coupling. (d) Minimum energy splitting (MES), defined as  $2\Omega = [\omega_+ - \omega_-]_{\min}$ , extracted from the results in (c).  $\Omega$  represents the plasmon-phonon coupling strength. The white dashed lines in (b) and (c) show the plasmon dispersion without the contribution of TMD phonons (SP<sup>2</sup>), for reference.

frequencies. In addition, the electric field of the acoustic plasmon mode becomes more localized between the two graphene layers, which is also demonstrated in the simulation shown in Sec. II C. It is important to point out that although the TMD layers have four nondegenerate optical phonon modes, only  $A_2''$  (IR) are out-of-plane IR-active phonon modes, as shown in Fig. 1(c). Due to the out-of-plane phonon vibrations and dipolarlike acoustic plasmon electric field mode,  $A_2''$  (IR) phonons match the acoustic plasmon mode perfectly to enhance the plasmon-phonon coupling between them.

#### B. The influence of the number of TMD layers on the plasmon-phonon coupling strength

Figure 4(a) shows the acoustic plasmon-phonon coupling strength  $\Omega$  as a function of the number of TMD layers ( $N$ ) in between the graphene monolayers, for  $E_F = 100$  meV. Blue

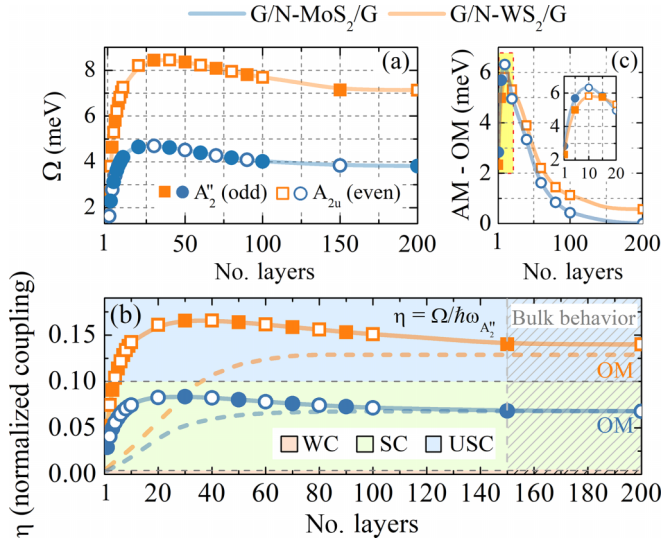


FIG. 4. Acoustic surface plasmon-phonon polaritons' (ASPPPs') coupling strength ( $\Omega$ ) as a function of the number of TMD layers ( $N$ ) in between two graphene monolayers [cf. Figs. 1(a) and 1(b)], for  $E_F = 100$  meV. Blue lines and dots (orange lines and squares) refer to  $N$ -MoS<sub>2</sub> ( $N$ -WS<sub>2</sub>) results. (a) Coupling energy between acoustic Dirac plasmon and the IR-active out-of-plane  $A_2''$  (solid symbols) and  $A_{2u}$  (open symbols) phonon modes, for odd and even number of layers, respectively. (b) ASPPPs' coupling strength normalized to the respective monolayer phonon frequencies at the  $\Gamma$  point defined as  $\eta = \Omega_{1(2)}/\hbar\omega_{A_2''}$ . Three different regions, blue, green, and pink, represent the WC ( $\eta < 0.01$ ), SC ( $0.01 \leq \eta < 0.1$ ), and USC ( $\eta \geq 0.1$ ) regime, respectively [75]. Blue and orange dashed lines are added for reference and represent the optical mode of a G/N-MX<sub>2</sub> vdWhs with  $E_F = 100$  meV [57]. The shaded area represents the bulk limit of the ASPPPs' coupling, reached for approximately 150 TMD layers. In this case, the acoustic plasmon mode converges approximately to the optical mode computed in Ref. [57], i.e., for a monolayer-graphene-based vdWhs. (c) Difference between the acoustic and optical normalized plasmon-phonon coupling in DLG-based vdWhs and monolayer-graphene-based vdWhs, respectively.

lines and symbols stand for G/N-MoS<sub>2</sub>/G results, while orange lines and symbols are for G/N-WS<sub>2</sub>/G. At first, the acoustic SPPPs' coupling ( $\Omega$ ) increases with the number of MX<sub>2</sub> layers, but after reaching a maximum value (i.e., near  $N = 25$  layers), it starts to slowly decrease, and finally converges to a value which is the bulk limit of this coupling parameter. The observed nonmonotonic trend is due to the interplay between the available phonon modes and the confined electric field induced by plasmon-plasmon interaction in the two graphene layers, which are two competing effects. With the increase of the number of MX<sub>2</sub> layers, more oscillators are involved, i.e., more phonons are available to couple with Dirac plasmons [81,82]. On the other hand, as the number of layers is increased further, the distance between the two graphene sheets increases, which leads to a weaker confined electric field between them. The two different coupling mechanisms, which depend on the phonon modes involved and the confined electric fields, will dominate in different ranges of the number of TMD layers and thus determine the relationship between coupling strength and the bulk limit.

### C. SPPP interaction: Weak-, strong-, and ultrastrong-coupling regimes vs the bulk limit

Figure 4(b) shows the normalized acoustic SPPPs' coupling  $\eta$  as a function of  $N$ -MoS<sub>2</sub> and  $N$ -WS<sub>2</sub> layers, where  $\eta = \Omega/\hbar\omega_{A_2''}$ , as defined by Kockum *et al.* [75], quantifies the coupling strength. Here,  $\omega_{A_2''}$  is the out-of-plane  $A_2''$  phonon frequency of a single TMD layer. The results, calculated in Ref. [57], for the coupling between optical plasmons (OM) arising from single-layer graphene and TMD phonons are shown in Fig. 4(b) as dashed blue (G/N-MoS<sub>2</sub>) and orange (G/N-WS<sub>2</sub>) lines, for comparison. For reference, three different regions, pink, green, and blue, are illustrated in Fig. 4(b) and represent the WC ( $\eta < 0.01$ ), SC ( $0.01 < \eta < 0.1$ ), and USC ( $\eta > 0.1$ ) regimes, respectively [75]. The acoustic SPPPs' coupling is stronger than the optical SPPPs' coupling in both MoS<sub>2</sub> and WS<sub>2</sub> vdWhs systems.

A remarkable result for this type of vdWhs, which is evident in Fig. 4(b), is the enhancement of the coupling between the acoustic Dirac plasmons and the IR-active out-of-plane  $A_2''$ , especially for few TMD layers, in contrast to the OM in the G/TMD system [57]. We consider that the bulk limit is reached for  $N > 150$ , as all results remain unchanged for larger  $N$ . In fact, the difference between the acoustic and optical plasmon-phonon coupling, defined as  $\Omega(\text{AM}) - \Omega(\text{OM})$ , which is illustrated in Fig. 4(c), exhibits a maximum around 10 TMDs layers (cf. the inset). Although the difference in the bulk limit for the MoS<sub>2</sub> case is not zero, which is related to the choice of the Fermi energy made for these calculations, this value is below 1 meV for 200 WS<sub>2</sub> layers. The effect of the Fermi energy on the plasmon-phonon coupling will be discussed in more detail later in this paper.

### D. Acoustic vs optical plasmon-phonon coupling in the bulk limit

Figure 5 illustrates the evolution of the acoustic and optical plasmon dispersions obtained from the QEH as the number of TMD layers is increased, in order to understand the bulk limit of the G/N-TMDs/G vdWhs. As follows from Figs. 5(a) and 5(b), calculated in a region close to the  $A_2''$  phonon frequency, increasing the number of TMD layers converges the OM and AM modes to the same curve, which corresponds to the plasmon mode in the bulk limit. In other words, while in Fig. 5(a), for G/50-MoS<sub>2</sub>/G, the loss function peaks for the top and bottom OM and AM are distinguishable, in Fig. 5(b), for G/150-MoS<sub>2</sub>/G, they form approximately degenerate SPPP modes. Figure 5(c) presents the plasmon dispersion curves for G/N-MoS<sub>2</sub>/G, with  $N = 10$  (green), 50 (orange), and 150 (blue), in the absence of phonon contributions, i.e., only taking into account the MoS<sub>2</sub> dielectric constant corresponding to each of the considered thicknesses. For reference, we calculated the plasmon dispersion for graphene on top of bulk MoS<sub>2</sub> using the QEH model, represented by the gray dash-dotted line in Fig. 5(c). One easily verifies that as the number of layers is increased, OM (solid lines) and AM (dotted lines) converge to each other and to the bulk limit (dash-dotted line), as expected.

### E. Effect of doping on the surface acoustic plasmon polaritons

The effects of gating or doping in vdWhs can be considered in a first approximation through a corresponding shift

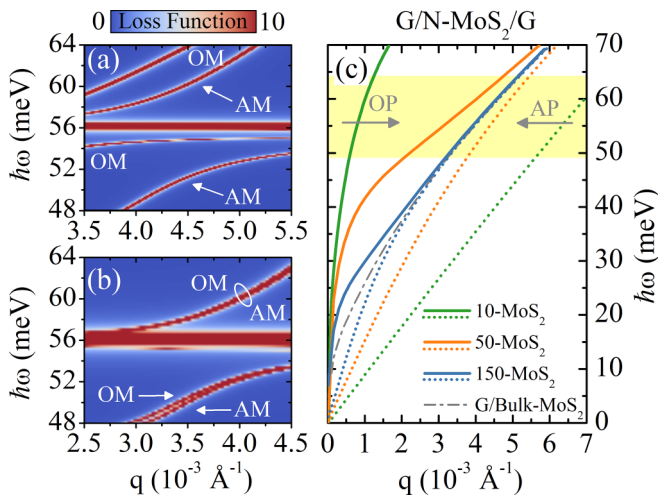


FIG. 5. (a) Loss function of SPPs for G/50-MoS<sub>2</sub>/G and (b) for G/150-MoS<sub>2</sub>/G, for  $E_F = 100$  meV. OM (AM) indicates the optical (acoustic) hybrid plasmon-phonon branch. (c) Acoustic SPPs' dispersion for G/N-MoS<sub>2</sub>/G in this case, considering just the dielectric contribution of the MoS<sub>2</sub> layers, i.e., disregarding the phonon contribution. Solid lines represent the optical plasmon dispersion and dotted lines stand for the acoustic plasmon dispersion. As the number of MoS<sub>2</sub> layers is increased, both the optical and acoustic plasmon dispersions converge to the bulk dispersion (gray dash-dotted line). The bulk dispersion was obtained for graphene on bulk MoS<sub>2</sub>, with  $E_F = 100$  meV. The yellow region in (c) corresponds to the frequency range of (a) and (b), emphasizing that for 150 MoS<sub>2</sub> layers, the OM and AM become completely indistinguishable.

of the Fermi energy. Figures 6(a) and 6(b) show how the graphene Fermi energy affects the coupling strength of the G/20-MoS<sub>2</sub>/G and G/20-WS<sub>2</sub>/G systems, respectively. The normalized coupling strength ( $\eta$ ) is calculated as a function of the Fermi energy ( $E_F$ ), which is considered the same in

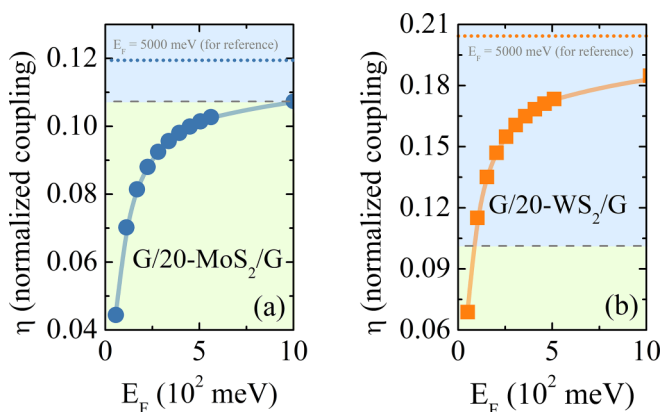


FIG. 6. Tuning the acoustic plasmon-phonon coupling strength  $\Omega$  by varying the Fermi energy simultaneously in the top ( $E_F^T = E_F$ ) and the bottom ( $E_F^B = E_F$ ) graphene layers. The acoustic SPPP coupling  $\Omega$  is shown as a function of the Fermi energy for (a) G/20-MoS<sub>2</sub>/G and (b) G/20-WS<sub>2</sub>/G. The blue [orange] dotted lines in (a) [(b)] are the reference of couplings for  $E_F = 5000$  meV. The green and blue regions represent SC ( $0.01 \leq \eta < 0.1$ ) and USC ( $\eta \geq 0.1$ ) regimes, respectively.

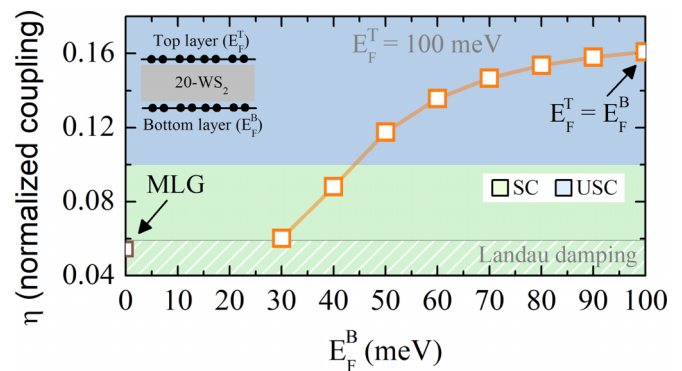


FIG. 7. Normalized coupling strength of acoustic SPPs in double-layer graphene intercalated by 20 layers of WS<sub>2</sub> (the inset shows a sketch of this system), as a function of the Fermi level of the bottom graphene layer  $E_F^B$ . For convenience, the top graphene Fermi energy is fixed at  $E_F^T = 100$  meV. For low  $E_F^B$ , the system behaves effectively as monolayer graphene over 20 WS<sub>2</sub> layers, where the acoustic SPPP is in the SC regime. The green and blue regions represent SC ( $0.01 \leq \eta < 0.1$ ) and USC ( $\eta \geq 0.1$ ) regimes, respectively.

both top and bottom graphene layers. As seen in the figure, in both cases, the coupling strength quickly increases to the USC regime with the increase of the Fermi energy, converging to a maximum value, represented by the dotted line. As explained in Ref. [57], for low Fermi energy, the Pauli blocking is lifted and interband single-particle processes are allowed. As a consequence, the plasmon lifetime is inhibited, thus suppressing the plasmon-phonon coupling. In addition, the plasmon frequencies increase with the doping of graphene. The dependence of the acoustic plasmon frequency  $\omega_{AM}(q)$  in the DLG system on the carrier density ( $n_e$ ) is  $\omega_{AM}(q) \sim (1/2)n_e^{1/4}$  [51], half of the one for single-layer graphene [83]. Since the Fermi energy in graphene is related to the carrier density through the relation  $n_e = (E_F/\hbar v_f)^2/\pi$ , at high doping levels, the change of the acoustic plasmon dispersion in the ( $q, \omega$ ) plane with the Fermi energy is not significant, which causes the flattening of the curve for high Fermi energy. Recent research has revealed that chemical doping introduces additional damping channels that can impact the plasmonic behavior of graphene [87]. Furthermore, doping also induces alterations in the phonon behavior of graphene [88,89], and thus the plasmonic response is modified via the plasmon-phonon coupling in graphene [90,91]. To mitigate this effect, it is crucial to ensure that the intrinsic graphene plasmon energy is lower than the optical phonons of graphene, which are around 0.2 eV [9,10,87]. Nevertheless, these results clearly show that the coupling strength can be conveniently tuned by doping.

Finally, we explore asymmetric doping, i.e., considering different Fermi energies for the top ( $E_F^T$ ) and bottom ( $E_F^B$ ) graphene layers (see inset in Fig. 7), to provide precise control of the coupling strength. To do so, we calculate the normalized coupling strength  $\eta$  for a G/20-WS<sub>2</sub>/G vdWhs, considering a fixed  $E_F^T = 100$  meV and varied values of  $E_F^B$ . Results are shown in Fig. 7. We observe that  $E_F^B < 30$  meV does not generate acoustic SPPs due to Landau damping; therefore, results will be discussed only for  $E_F^B > 30$  meV. As expected,

when  $E_F^B$  is low, the normalized coupling strength has almost the same value as that for a G/20-WS<sub>2</sub> monolayer-graphene system (shown under the label MLG in Fig. 7, for comparison), which is in the SC regime. However, as  $E_F^B$  increases, the normalized coupling strength crosses from the SC to the USC regime at  $E_F^B \approx 45$  meV, which gives a guideline to precisely fine tune the coupling strength by doping, which can be achieved even electronically, by gate voltage [31].

#### IV. CONCLUSIONS

We have demonstrated the possibility of tuning the coupling strength of the acoustic graphene plasmons in a double-layer graphene (DLG) with the IR-active out-of-plane  $A_2''$  phonon modes of the  $N$  intercalated layers of MoS<sub>2</sub> or WS<sub>2</sub>, thereby enabling precise control over the coupling regime, ranging from weak all the way to ultrastrong coupling. The strong interaction between the plasmonic and phononic modes in such G/ $N$ -MX<sub>2</sub>/G heterostructures leads to the formation of hybrid excitations with unique optical and electronic properties. Our findings show that for a limited number of TMD layers, the coupling strength between acoustic plasmons and phonons in DLG-based van der Waals heterostructures surpasses that of optical plasmons in monolayer-graphene-based heterostructures, discussed earlier. Our numerical simulations reveal a peak at  $N = 10$  layers that differs 6 meV between single- and double-layer cases. This is due to the dipolelike nature of acoustic graphene plasmons, as explained in Sec. II C.

Our calculations also show that for  $E_F = 100$  meV, the coupling energy converges to a constant (bulk limit) for a number of TMD layers larger than  $N = 150$ , where the acoustic and optical plasmon-phonon couplings converge to the same value, which is also verified by comparing the loss

functions of G/50-MoS<sub>2</sub>/G and G/150-MoS<sub>2</sub>/G. In the latter, one can no longer distinguish between the optical and acoustic plasmon dispersions since the top and bottom graphene layers are far apart.

Finally, we discussed the effect of doping on the surface acoustic plasmon polaritons, changing the Fermi energy in both the top ( $E_F^T$ ) and bottom ( $E_F^B$ ) graphene layers of the studied G/ $N$ -MX<sub>2</sub>/G heterostructures. We have demonstrated that different values of  $E_F^T$  and  $E_F^B$  enable one to tune the coupling parameter from strong to ultrastrong coupling regimes, thus rendering such asymmetric doping a fine adjustment knob for the coupling regimes of this system. Even though we presented results only for two selected TMD materials, our findings are easily transferable for plasmon-phonon coupling phenomena in different DLG-based vdWhs. The precise yet broad tuning of coupling found here, ranging from weak to ultrastrong regimes, may be a key achievement towards novel nanothermoelectronics and on-chip optical devices, as well as further breakthroughs in understanding the behavior of materials at the nanoscale.

The data that support the findings of this study will be made available by the authors upon reasonable request.

#### ACKNOWLEDGMENTS

We thank N. F. Jiao, B. Van Duppen, and J. D. P. de Sousa for useful discussions. This work was supported by the Brazilian Council for Research (CNPq), through the UNIVERSAL and PQ programs, by the Brazilian National Council for the Improvement of Higher Education (CAPES), and by the Research Foundation - Flanders (FWO). Z.H.T. gratefully acknowledges support from the China Scholarship Council (CSC).

- 
- [1] K. S. Novoselov, V. I. Fal'ko, L. Colombo, P. R. Gellert, M. G. Schwab, and K. Kim, A roadmap for graphene, *Nature (London)* **490**, 192 (2012).
  - [2] K. S. Novoselov, A. K. Geim, S. V. Morozov, D. Jiang, Y. Zhang, S. V. Dubonos, I. V. Grigorieva, and A. A. Firsov, Electric field effect in atomically thin carbon films, *Science* **306**, 666 (2004).
  - [3] A. N. Grigorenko, M. Polini, and K. S. Novoselov, Graphene plasmonics, *Nat. Photon.* **6**, 749 (2012).
  - [4] P. A. D. Gonçalves and N. M. R. Peres, *An Introduction to Graphene Plasmonics* (World Scientific, Singapore, 2015).
  - [5] J. Chen, M. Badioli, P. Alonso-González, S. Thongrattanasiri, F. Huth, J. Osmond, M. Spasenović, A. Centeno, A. Pesquera, P. Godignon *et al.*, Optical nano-imaging of gate-tunable graphene plasmons, *Nature (London)* **487**, 77 (2012).
  - [6] Z. Fei, A. Rodin, G. O. Andreev, W. Bao, A. McLeod, M. Wagner, L. Zhang, Z. Zhao, M. Thiemens, G. Dominguez *et al.*, Gate-tuning of graphene plasmons revealed by infrared nano-imaging, *Nature (London)* **487**, 82 (2012).
  - [7] L. Ju, B. Geng, J. Horng, C. Girit, M. Martin, Z. Hao, H. A. Bechtel, X. Liang, A. Zettl, Y. R. Shen *et al.*, Graphene plasmonics for tunable terahertz metamaterials, *Nat. Nanotechnol.* **6**, 630 (2011).
  - [8] Z. Fei, G. O. Andreev, W. Bao, L. M. Zhang, A. S. McLeod, C. Wang, M. K. Stewart, Z. Zhao, G. Dominguez, M. Thiemens *et al.*, Infrared nanoscopy of dirac plasmons at the graphene-SiO<sub>2</sub> interface, *Nano Lett.* **11**, 4701 (2011).
  - [9] H. Yan, T. Low, W. Zhu, Y. Wu, M. Freitag, X. Li, F. Guinea, P. Avouris, and F. Xia, Damping pathways of mid-infrared plasmons in graphene nanostructures, *Nat. Photon.* **7**, 394 (2013).
  - [10] M. Jablan, H. Buljan, and M. Soljačić, Plasmonics in graphene at infrared frequencies, *Phys. Rev. B* **80**, 245435 (2009).
  - [11] Y. Zhong, S. D. Malagari, T. Hamilton, and D. M. Wasserman, Review of mid-infrared plasmonic materials, *J. Nanophoton.* **9**, 093791 (2015).
  - [12] J. A. Schuller, E. S. Barnard, W. Cai, Y. C. Jun, J. S. White, and M. L. Brongersma, Plasmonics for extreme light concentration and manipulation, *Nat. Mater.* **9**, 193 (2010).
  - [13] T. Low and P. Avouris, Graphene plasmonics for terahertz to mid-infrared applications, *ACS Nano* **8**, 1086 (2014).
  - [14] M. Polini, Tuning terahertz lasers via graphene plasmons, *Science* **351**, 229 (2016).
  - [15] P. Alonso-González, A. Y. Nikitin, Y. Gao, A. Woessner, M. B. Lundeberg, A. Principi, N. Forcellini, W. Yan, S. Vélez, A. Huber *et al.*, Acoustic terahertz graphene plasmons revealed by photocurrent nanoscopy, *Nat. Nanotechnol.* **12**, 31 (2017).

- [16] A. K. Geim and I. V. Grigorieva, Van der Waals heterostructures, *Nature (London)* **499**, 419 (2013).
- [17] K. S. Novoselov, A. Mishchenko, A. Carvalho, and A. H. Castro Neto, 2d materials and van der waals heterostructures, *Science* **353**, aac9439 (2016).
- [18] Y. Liu, N. O. Weiss, X. Duan, H.-C. Cheng, Y. Huang, and X. Duan, Van der Waals heterostructures and devices, *Nat. Rev. Mater.* **1**, 16042 (2016).
- [19] Q. H. Wang, K. Kalantar-Zadeh, A. Kis, J. N. Coleman, and M. S. Strano, Electronics and optoelectronics of two-dimensional transition metal dichalcogenides, *Nat. Nanotechnol.* **7**, 699 (2012).
- [20] D. Jariwala, V. K. Sangwan, L. J. Lauhon, T. J. Marks, and M. C. Hersam, Emerging device applications for semiconducting two-dimensional transition metal dichalcogenides, *ACS Nano* **8**, 1102 (2014).
- [21] H. Zhang, Ultrathin two-dimensional nanomaterials, *ACS Nano* **9**, 9451 (2015).
- [22] K. F. Mak and J. Shan, Photonics and optoelectronics of 2d semiconductor transition metal dichalcogenides, *Nat. Photon.* **10**, 216 (2016).
- [23] Y. Gong, J. Lin, X. Wang, G. Shi, S. Lei, Z. Lin, X. Zou, G. Ye, R. Vajtai, B. I. Yakobson *et al.*, Vertical and in-plane heterostructures from ws 2/mos 2 monolayers, *Nat. Mater.* **13**, 1135 (2014).
- [24] S. Manzeli, D. Ovchinnikov, D. Pasquier, O. V. Yazyev, and A. Kis, 2D transition metal dichalcogenides, *Nat. Rev. Mater.* **2**, 17033 (2017).
- [25] V. O. Özçelik, J. G. Azadani, C. Yang, S. J. Koester, and T. Low, Band alignment of two-dimensional semiconductors for designing heterostructures with momentum space matching, *Phys. Rev. B* **94**, 035125 (2016).
- [26] P. K. Sahoo, S. Memaran, Y. Xin, L. Balicas, and H. R. Gutiérrez, One-pot growth of two-dimensional lateral heterostructures via sequential edge-epitaxy, *Nature (London)* **553**, 63 (2018).
- [27] X. Duan, C. Wang, J. C. Shaw, R. Cheng, Y. Chen, H. Li, X. Wu, Y. Tang, Q. Zhang, A. Pan *et al.*, Lateral epitaxial growth of two-dimensional layered semiconductor heterojunctions, *Nat. Nanotechnol.* **9**, 1024 (2014).
- [28] Y. Gong, S. Lei, G. Ye, B. Li, Y. He, K. Keyshar, X. Zhang, Q. Wang, J. Lou, Z. Liu *et al.*, Two-step growth of two-dimensional WSe<sub>2</sub>/MoSe<sub>2</sub> heterostructures, *Nano Lett.* **15**, 6135 (2015).
- [29] C. Huang, S. Wu, A. M. Sanchez, J. J. Peters, R. Beanland, J. S. Ross, P. Rivera, W. Yao, D. H. Cobden, and X. Xu, Lateral heterojunctions within monolayer MoSe<sub>2</sub>-WSe<sub>2</sub> semiconductors, *Nat. Mater.* **13**, 1096 (2014).
- [30] D. Jariwala, T. J. Marks, and M. C. Hersam, Mixed-dimensional van der Waals heterostructures, *Nat. Mater.* **16**, 170 (2017).
- [31] K. S. Novoselov, D. Jiang, F. Schedin, T. Booth, V. Khotkevich, S. Morozov, and A. K. Geim, Two-dimensional atomic crystals, *Proc. Natl. Acad. Sci.* **102**, 10451 (2005).
- [32] Y. Liu, T. X. Gong, Y. N. Zheng, X. W. Wang, J. Xu, Q. Q. Ai, J. X. Guo, W. Huang, S. F. Zhou, Z. W. Liu *et al.*, Ultra-sensitive and plasmon-tunable graphene photodetectors for micro-spectrometry, *Nanoscale* **10**, 20013 (2018).
- [33] B. Shan, L. Xia, S. P. Ma, Z. h. Yin, X. Y. Liu, G. H. Li, and Y. Huang, Achieving multiband compatible and mechanical tuning absorber using edge topological defect-induced graphene plasmon, *Carbon* **192**, 1 (2022).
- [34] X. S. Liu, G. Q. Liu, P. Tang, G. L. Fu, G. Z. Du, Q. Q. Chen, and Z. Q. Liu, Quantitatively optical and electrical-adjusting high-performance switch by graphene plasmonic perfect absorbers, *Carbon* **140**, 362 (2018).
- [35] Z. P. Sun, A. Martinez, and F. Wang, Optical modulators with 2D layered materials, *Nat. Photon.* **10**, 227 (2016).
- [36] Y. H. Ding, X. W. Guan, X. L. Zhu, H. Hu, S. I. Bozhevolnyi, L. K. Oxenløwe, K. J. Jin, N. A. Mortensen, and S. S. Xiao, Efficient electro-optic modulation in low-loss graphene-plasmonic slot waveguides, *Nanoscale* **9**, 15576 (2017).
- [37] Y. L. Li, H. G. Yan, D. B. Farmer, X. Meng, W. J. Zhu, R. M. Osgood, T. F. Heinz, and P. Avouris, Graphene plasmon enhanced vibrational sensing of surface-adsorbed layers, *Nano Lett.* **14**, 1573 (2014).
- [38] A. Marini, I. Silveiro, and F. J. García de Abajo, Molecular sensing with tunable graphene plasmons, *ACS Photon.* **2**, 876 (2015).
- [39] M. B. Lundberg, Y. Gao, R. Asgari, C. Tan, B. Van Duppen, M. Autore, P. Alonso-González, A. Woessner, K. Watanabe, T. Taniguchi *et al.*, Tuning quantum nonlocal effects in graphene plasmonics, *Science* **357**, 187 (2017).
- [40] M. B. Lundberg, Y. Gao, A. Woessner, C. Tan, P. Alonso-González, K. Watanabe, T. Taniguchi, J. Hone, R. Hillenbrand, and F. H. L. Koppens, Thermoelectric detection and imaging of propagating graphene plasmons, *Nat. Mater.* **16**, 204 (2017).
- [41] A. Woessner, M. B. Lundberg, Y. Gao, A. Principi, P. Alonso-González, M. Carrega, K. Watanabe, T. Taniguchi, G. Vignale, M. Polini *et al.*, Highly confined low-loss plasmons in graphene–boron nitride heterostructures, *Nat. Mater.* **14**, 421 (2015).
- [42] Z. Fei, E. Iwinski, G. Ni, L. Zhang, W. Bao, A. Rodin, Y. Lee, M. Wagner, M. Liu, S. Dai *et al.*, Tunneling plasmonics in bilayer graphene, *Nano Lett.* **15**, 4973 (2015).
- [43] S. Dai, Q. Ma, M. Liu, T. Andersen, Z. Fei, M. Goldflam, M. Wagner, K. Watanabe, T. Taniguchi, M. Thiemens *et al.*, Graphene on hexagonal boron nitride as a tunable hyperbolic metamaterial, *Nat. Nanotechnol.* **10**, 682 (2015).
- [44] S. Dai, Z. Fei, Q. Ma, A. Rodin, M. Wagner, A. McLeod, M. Liu, W. Gannett, W. Regan, K. Watanabe *et al.*, Tunable phonon polaritons in atomically thin van der Waals crystals of boron nitride, *Science* **343**, 1125 (2014).
- [45] X. Zhang, X. F. Qiao, W. Shi, J. B. Wu, D. S. Jiang, and P. H. Tan, Phonon and Raman scattering of two-dimensional transition metal dichalcogenides from monolayer, multilayer to bulk material, *Chem. Soc. Rev.* **44**, 2757 (2015).
- [46] J. Xia, J. Yan, and Z. X. Shen, Transition metal dichalcogenides: Structural, optical and electronic property tuning via thickness and stacking, *FlatChem* **4**, 1 (2017).
- [47] C. Ataca, M. Topsakal, E. Aktürk, and S. Ciraci, A comparative study of lattice dynamics of three- and two-dimensional MoS<sub>2</sub>, *J. Phys. Chem. C* **115**, 16354 (2011).
- [48] R. Y. Liu, L. X. Ge, H. Y. Yu, Z. Cui, and X. H. Wu, Near-field radiative heat transfer via coupling graphene plasmons with different phonon polaritons in the reststrahlen bands, *Engineer. Sci.* **18**, 224 (2021).
- [49] X. H. Wu and R. Y. Liu, Near-field radiative heat transfer between graphene covered biaxial hyperbolic materials, *ES Energy Environ.* **10**, 66 (2020).

- [50] L. Lu, B. Zhang, H. Ou, B. W. Li, K. Zhou, J. L. Song, Z. X. Luo, and Q. Cheng, Enhanced near-field radiative heat transfer between graphene/hbn systems, *Small* **18**, 2108032 (2022).
- [51] E. H. Hwang and S. Das Sarma, Plasmon modes of spatially separated double-layer graphene, *Phys. Rev. B* **80**, 205405 (2009).
- [52] T. Vazifeshenas, T. Amlaki, M. Farmanbar, and F. Parhizgar, Temperature effect on plasmon dispersions in double-layer graphene systems, *Phys. Lett. A* **374**, 4899 (2010).
- [53] R. E. V. Profumo, R. Asgari, M. Polini, and A. H. MacDonald, Double-layer graphene and topological insulator thin-film plasmons, *Phys. Rev. B* **85**, 085443 (2012).
- [54] K. A. Guerrero-Becerra, A. Tomadin, and M. Polini, Electrical plasmon injection in double-layer graphene heterostructures, *Phys. Rev. B* **100**, 125434 (2019).
- [55] N. Van Men, N. Q. Khanh, and D. T. K. Phuong, Plasmon modes in double-layer gapped graphene, *Physica E* **118**, 113859 (2020).
- [56] S. G. Menabde, I. H. Lee, S. Lee, H. Ha, J. T. Heiden, D. Yoo, T. T. Kim, T. Low, Y. H. Lee, S. H. Oh *et al.*, Real-space imaging of acoustic plasmons in large-area graphene grown by chemical vapor deposition, *Nat. Commun.* **12**, 938 (2021).
- [57] I. R. Lavour, A. Chaves, F. M. Peeters, and B. Van Duppen, Tunable coupling of terahertz dirac plasmons and phonons in transition-metal dichalcogenide-based van der Waals heterostructures, *2D Mater.* **9**, 015018 (2022).
- [58] C. Hu, A. Deng, P. Shen, X. Luo, X. Zhou, T. Wu, X. Huang, Y. Dong, K. Watanabe, T. Taniguchi *et al.*, Direct imaging of interlayer-coupled symmetric and antisymmetric plasmon modes in graphene/hbn/graphene heterostructures, *Nanoscale* **13**, 14628 (2021).
- [59] Z. H. Tao, H. M. Dong, Y. F. Duan, J. L. Liu, and B. H. Cao, Tunable coupled terahertz surface plasmon polaritons in graphene metamaterials, *J. Opt.* **21**, 045107 (2019).
- [60] P. A. D. Gonçalves and N. M. R. Peres, *An Introduction to Graphene Plasmonics* (World Scientific, Singapore, 2016).
- [61] G. V. Gabriele Giuliani, *Quantum Theory of the Electron Liquid* (Cambridge University Press, Cambridge, 2008).
- [62] A. L. Fetter, *Quantum Theory of Many-Particle Systems* (Dover, Mineola, NY, 2003).
- [63] S. M. Badalyan and F. M. Peeters, Effect of nonhomogeneous dielectric background on the plasmon modes in graphene double-layer structures at finite temperatures, *Phys. Rev. B* **85**, 195444 (2012).
- [64] K. Andersen, S. Latini, and K. S. Thygesen, Dielectric genome of van der Waals heterostructures, *Nano Lett.* **15**, 4616 (2015).
- [65] M. N. Gjerding, L. S. R. Cavalcante, A. Chaves, and K. S. Thygesen, Efficient *ab initio* modeling of dielectric screening in 2D van der Waals materials: Including phonons, substrates, and doping, *J. Phys. Chem. C* **124**, 11609 (2020).
- [66] L. S. R. Cavalcante, M. N. Gjerding, A. Chaves, and K. S. Thygesen, Enhancing and controlling plasmons in Janus mosse-graphene based van der Waals heterostructures, *J. Phys. Chem. C* **123**, 16373 (2019).
- [67] I. R. Lavour, L. S. R. Cavalcante, A. Chaves, F. M. Peeters, and B. Van Duppen, Probing the structure and composition of van der Waals heterostructures using the nonlocality of dirac plasmons in the terahertz regime, *2D Mater.* **8**, 015014 (2020).
- [68] S. N. Shirodkar, M. Mattheakis, P. Cazeaux, P. Narang, M. Soljačić, and E. Kaxiras, Quantum plasmons with optical-range frequencies in doped few-layer graphene, *Phys. Rev. B* **97**, 195435 (2018).
- [69] H. C. Nerl, K. T. Winther, F. S. Hage, K. S. Thygesen, L. Houben, C. Backes, J. N. Coleman, Q. M. Ramasse, and V. Nicolosi, Probing the local nature of excitons and plasmons in few-layer MoS<sub>2</sub>, *npj 2D Mater. Appl.* **1**, 2 (2017).
- [70] S. Haastrup, M. Strange, M. Pandey, T. Deilmann, P. S. Schmidt, N. F. Hinsche, M. N. Gjerding, D. Torelli, P. M. Larsen, A. C. Riis-Jensen *et al.*, The computational 2D materials database: High-throughput modeling and discovery of atomically thin crystals, *2D Mater.* **5**, 042002 (2018).
- [71] M. N. Gjerding, A. Taghizadeh, A. Rasmussen, S. Ali, F. Bertoldo, T. Deilmann, N. R. Knøsgaard, M. Kruse, A. H. Larsen, S. Manti *et al.*, Recent progress of the computational 2D materials database (C2DB), *2D Mater.* **8**, 044002 (2021).
- [72] The dielectric building blocks and QEH software can be downloaded at <https://cmr.fysik.dtu.dk/vdwh/vdwh.html>.
- [73] P. Törmä and W. L. Barnes, Strong coupling between surface plasmon polaritons and emitters: A review, *Rep. Prog. Phys.* **78**, 013901 (2014).
- [74] O. Bitton, S. N. Gupta, and G. Haran, Quantum dot plasmonics: From weak to strong coupling, *Nanophotonics* **8**, 559 (2019).
- [75] A. Frisk Kockum, A. Miranowicz, S. De Liberato, S. Savasta, and F. Nori, Ultrastrong coupling between light and matter, *Nat. Rev. Phys.* **1**, 19 (2019).
- [76] X. Zhong, T. Chervy, S. Wang, J. George, A. Thomas, J. A. Hutchison, E. Devaux, C. Genet, and T. W. Ebbesen, Non-radiative energy transfer mediated by hybrid light-matter states, *Angew. Chem.* **128**, 6310 (2016).
- [77] E. Orgiu, J. George, J. Hutchison, E. Devaux, J. Dayen, B. Doudin, F. Stellacci, C. Genet, J. Schachenmayer, C. Genes *et al.*, Conductivity in organic semiconductors hybridized with the vacuum field, *Nat. Mater.* **14**, 1123 (2015).
- [78] Note that the deep-strong-coupling (DSC) regime, recently achieved in experiments involving crystals of nanoparticles [92], exhibits plasmon-phonon couplings even stronger than those observed in the system of our investigation.
- [79] Z. H. Tao, H. M. Dong, M. V. Milošević, F. M. Peeters, and B. Van Duppen, Tailoring Dirac Plasmons via Anisotropic Dielectric Environment by Design, *Phys. Rev. Appl.* **16**, 054030 (2021).
- [80] V. Gusynin, S. Sharapov, and J. Carbotte, Magneto-optical conductivity in graphene, *J. Phys.: Condens. Matter* **19**, 026222 (2007).
- [81] Y. C. Jia, H. Zhao, Q. S. Guo, X. M. Wang, H. Wang, and F. N. Xia, Tunable plasmon-phonon polaritons in layered graphene-hexagonal boron nitride heterostructures, *ACS Photon.* **2**, 907 (2015).
- [82] C. Huck, J. Vogt, T. Neuman, T. Nagao, R. Hillenbrand, J. Aizpurua, A. Pucci, and F. Neubrech, Strong coupling between phonon-polaritons and plasmonic nanorods, *Opt. Express* **24**, 25528 (2016).
- [83] H. M. Dong, L. L. Li, W. Y. Wang, S. H. Zhang, C. X. Zhao, and W. Xu, Terahertz plasmon and infrared coupled plasmon-phonon modes in graphene, *Physica E* **44**, 1889 (2012).
- [84] W. J. Zhao, Z. Ghorannevis, K. K. Amara, J. R. Pang, M. Toh, X. Zhang, C. Kloc, P. H. Tan, and G. Eda, Lattice dynamics in

- mono- and few-layer sheets of WS<sub>2</sub> and WSe<sub>2</sub>, *Nanoscale* **5**, 9677 (2013).
- [85] A. Molina-Sánchez and L. Wirtz, Phonons in single-layer and few-layer MoS<sub>2</sub> and WS<sub>2</sub>, *Phys. Rev. B* **84**, 155413 (2011).
- [86] B. Peng, H. Zhang, H. Z. Shao, Y. C. Xu, X. C. Zhang, and H. Y. Zhu, Thermal conductivity of monolayer MoS<sub>2</sub>, MoSe<sub>2</sub>, and WS<sub>2</sub>: Interplay of mass effect, interatomic bonding and anharmonicity, *RSC Adv.* **6**, 5767 (2016).
- [87] D. Novko, Dopant-induced plasmon decay in graphene, *Nano Lett.* **17**, 6991 (2017).
- [88] E. Cappelluti, L. Benfatto, M. Manzardo, and A. B. Kuzmenko, Charged-phonon theory and fano effect in the optical spectroscopy of bilayer graphene, *Phys. Rev. B* **86**, 115439 (2012).
- [89] A. B. Kuzmenko, L. Benfatto, E. Cappelluti, I. Crassee, D. van der Marel, P. Blake, K. S. Novoselov, and A. K. Geim, Gate Tunable Infrared Phonon Anomalies in Bilayer Graphene, *Phys. Rev. Lett.* **103**, 116804 (2009).
- [90] F. J. Bezares, A. D. Sanctis, J. Saavedra, A. Woessner, P. Alonso-González, I. Amenabar, J. Chen, T. H. Bointon, S. Dai, M. M. Fogler *et al.*, Intrinsic plasmon-phonon interactions in highly doped graphene: A near-field imaging study, *Nano Lett.* **17**, 5908 (2017).
- [91] E. H. Hwang, R. Sensarma, and S. Das Sarma, Plasmon-phonon coupling in graphene, *Phys. Rev. B* **82**, 195406 (2010).
- [92] N. S. Mueller, Y. Okamura, B. G. Vieira, S. Juergensen, H. Lange, E. B. Barros, F. Schulz, and S. Reich, Deep strong light-matter coupling in plasmonic nanoparticle crystals, *Nature (London)* **583**, 780 (2020).
- [93] A. Berkdemir, H. R. Gutiérrez, A. R. Botello-Méndez, N. Perea-López, A. L. Elías, C. I. Chia, B. Wang, V. H. Crespi, F. López-Urías, J. C. Charlier *et al.*, Identification of individual and few layers of WS<sub>2</sub> using raman spectroscopy, *Sci. Rep.* **3**, 1755 (2013).
- [94] A. Sengupta, A. Chanana, and S. Mahapatra, Phonon scattering limited performance of monolayer MoS<sub>2</sub> and WSe<sub>2</sub> n-MOSFET, *AIP Adv.* **5**, 027101 (2015).
- Correction:* Two equation numbers were miset during the proof conversion process in the first complete sentence after Eq. (5) and have been fixed.